

Multi-View Hypercomplex Learning for Breast Cancer Screening

Eleonora Lopez, *Graduate Student Member, IEEE*, Eleonora Grassucci, *Graduate Student Member, IEEE*,
Martina Valleriani, and Danilo Comminiello, *Senior Member, IEEE*

Abstract—Traditionally, deep learning methods for breast cancer classification perform a single-view analysis. However, radiologists simultaneously analyze all four views that compose a mammography exam, owing to the correlations contained in mammography views, which present crucial information for identifying tumors. In light of this, some studies have started to propose multi-view methods. Nevertheless, in such existing architectures, mammogram views are processed as independent images by separate convolutional branches, thus losing correlations among them. To overcome such limitations, in this paper, we propose a methodological approach for multi-view breast cancer classification based on parameterized hypercomplex neural networks. Thanks to hypercomplex algebra properties, our networks are able to model, and thus leverage, existing correlations between the different views that comprise a mammogram, thus mimicking the reading process performed by clinicians. This happens because hypercomplex networks capture both global properties, as standard neural models, as well as local relations, i.e., inter-view correlations, which real-valued networks fail at modeling. We define architectures designed to process two-view exams, namely PHResNets, and four-view exams, i.e., PHYSEnet and PHYBOnet. Through an extensive experimental evaluation conducted with publicly available datasets, we demonstrate that our proposed models clearly outperform real-valued counterparts and state-of-the-art methods, proving that breast cancer classification benefits from the proposed multi-view architectures. We also assess the method generalizability beyond mammogram analysis by considering different benchmarks, as well as a finer-scaled task such as segmentation. Full code and pretrained models for complete reproducibility of our experiments are freely available at <https://github.com/ispamm/PHBreast>.

Index Terms—Multi-View Learning, Hypercomplex Neural Networks, Hypercomplex Algebra, Breast Cancer Screening

I. INTRODUCTION

Among the different types of cancer that affect women worldwide, breast cancer alone accounts for almost one-third, making it by far the cancer with highest incidence among women [1]. For this reason, early detection of this disease is of extreme importance and, to this end, screening mammography is performed annually on all women above a certain age [2], [3]. During a mammography exam, two views of the breast are taken, thus capturing it from above, i.e., the craniocaudal (CC) view, and from the side, i.e., the mediolateral oblique (MLO) view. More in detail, the CC and MLO views of the same breast are known as ipsilateral views, while the same view of both breasts as bilateral views. Importantly, when reading a mammogram, radiologists examine the views by performing a

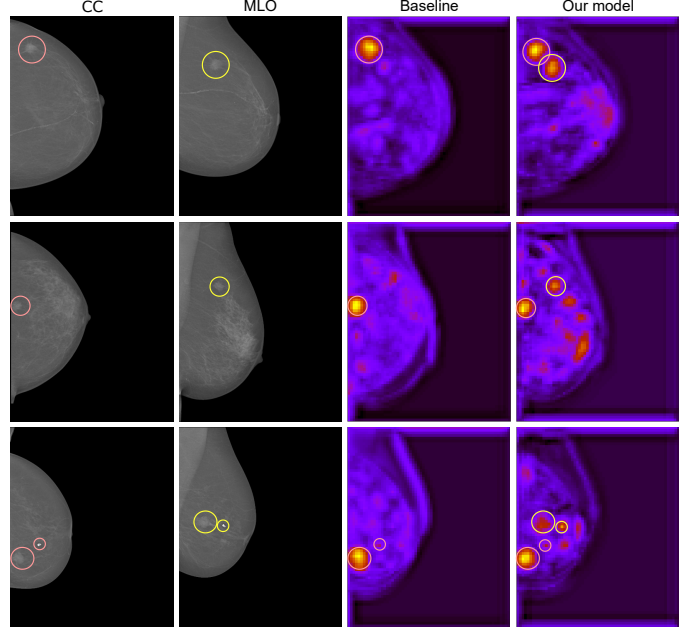


Fig. 1. Visualization of hypercomplex multi-view learning. In the figure, there are the two views (CC and MLO) corresponding to one breast containing a malignant mass (highlighted in red and green in the respective views). Then, we show the activation maps of a baseline, i.e. the real-valued counterpart of our network (SEnet), and the proposed hypercomplex architecture (PHYSEnet). Unlike the network in the real domain, ours learns from both views as it is visible that there are highlighted areas corresponding to both views.

double comparison, that is comparing ipsilateral views along with bilateral views, as each comparison provides valuable information. Such multi-view analysis has been found to be essential in order to make an accurate diagnosis of breast cancer [4], [5].

Recently, many works are employing deep learning (DL)-based methods in the medical field and, especially, for breast cancer classification and detection with encouraging results [6]–[17]. Inspired by the multi-view analysis performed by radiologists, several recent studies try to adopt a multi-view architecture in order to obtain a more robust and performing model [18]–[29].

The general approach taken by these works consists in designing a neural network with different branches dedicated to processing the different views. However, there are several issues associated with this procedure. To begin with, a recent study [19] observes that this kind of model can favor one of the two views during learning, thus not truly taking advantage of the multi-view input. Additionally, the model might fail

Authors are with the Department of Information Engineering, Electronics and Telecommunications (DIET), Sapienza University of Rome, Italy. Corresponding author’s email: eleonora.lopez@uniroma1.it.

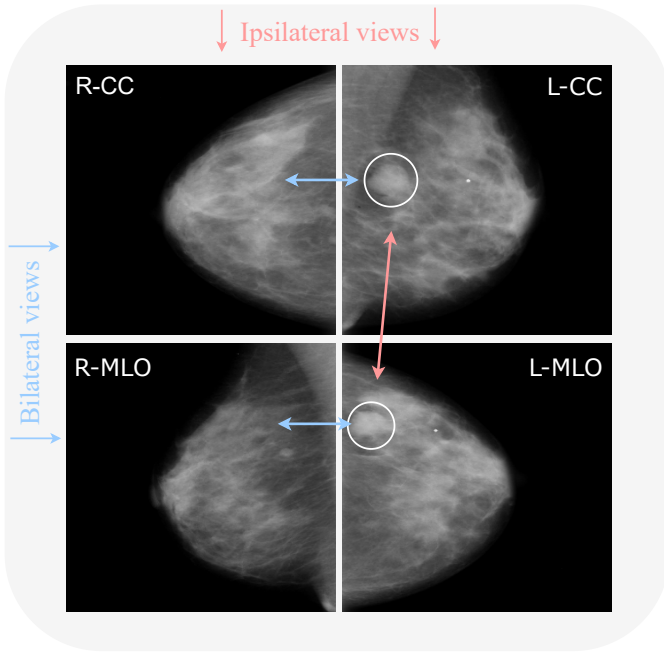


Fig. 2. Example of a mammography exam from the CBIS-DDSM dataset with the four views: left CC (L-CC), right CC (R-CC), left MLO (L-MLO), and right MLO (R-MLO). Horizontal couples are bilateral views (blue), while vertical couples are ipsilateral views (red). Arrows indicate the relations among views. Bilateral relations reveal an asymmetry (as there is a mass on the left that is not present on the right). Ipsilateral relations give a better view of the specific mass.

entirely in leveraging the correlated views and actually worsen the performance with respect to its single-view counterpart [19], [30]. Thus, it is made clear that improving the ability of deep networks to truly exploit the information contained in multiple views is still a largely open research question. To address and overcome these problems, we employ a novel technique in deep learning that relies on exotic algebraic systems, such as quaternions and, more in general, hypercomplex ones.

In recent years, quaternion neural networks (QNNs) have gained a lot of interest in a variety of applications [31]–[36]. The reason for this is the particular properties that characterize these models. As a matter of fact, thanks to the quaternion algebra rules on which these models are based (e.g., the Hamilton product), quaternion networks possess the capability of modeling interactions between input channels. Thus, they capture internal latent relations within them and additionally reduce the total number of parameters by 75%, while still attaining comparable performance to their real-valued counterparts. Furthermore, built upon the idea of QNNs, the recent parameterized hypercomplex neural networks (PHNNs) generalize hypercomplex multiplications as a sum of n Kronecker products, where n is a hyperparameter that controls in which domain the model operates [37], [38], going beyond quaternion algebra. Thus, they improve previous shortcomings by making these models applicable to any n -dimensional input (instead of just 3D/4D as the quaternion domain) thanks to the introduction of the parameterized hypercomplex multiplication (PHM) and convolutional (PHC) layer [37], [38].

Motivated by the problems mentioned above and the benefits of hypercomplex models, we propose a framework of multi-view learning for breast cancer classification based on PHNNs, taking a completely different approach with respect to the literature. More in detail, we propose a family of parameterized hypercomplex ResNets (PHResNets) able to process ipsilateral views corresponding to one breast, i.e., two views. Additionally, we design two parameterized hypercomplex networks for four views, namely PHYBONet and PHYSEnet. PHYBONet involves a bottleneck with $n = 4$ to process learned features in a joint fashion, performing a patient-level analysis. Instead, PHYSEnet is characterized by a shared encoder with $n = 2$ to learn stronger representations of the ipsilateral views by sharing the weights between bilateral ones, focusing on a breast-level analysis.

The advantages of our approach are manifold. Firstly, instead of handling the mammographic views independently, which results in losing significant correlations, our models process them as a unique component, without breaking the original nature of the exam. Secondly, thanks to hypercomplex algebra properties, the proposed models are endowed with the capability of preserving existing latent relations between views by modeling and capturing their interactions, as shown in Fig. 1. In fact, hypercomplex networks have been shown to effectively model not only global relations as standard deep learning networks but also local relations [32]. In the context of the mammography exam, these local relations are essential since they represent the complementary information contained in the multiple views, which are critical for a correct diagnosis and represent a fundamental step of the reading process performed by radiologists [4], [5]. In this sense, with the proposed approach in the hypercomplex domain, we can say that our networks mimic the examination process of radiologists in real-life settings. Thirdly, our parameterized hypercomplex networks are characterized by the number of free parameters *halved*, when $n = 2$, and reduced by $1/4$, when $n = 4$, with respect to their real-valued counterparts. Finally, our proposed approach is both portable and flexible. It can be seamlessly applied to other medical exams involving multiple views or modalities, signifying its portability. Furthermore, any neural network can be easily defined within the hypercomplex domain by simply integrating PHC layers, thus highlighting its flexibility. To the best of our knowledge, this is the first time that hypercomplex models have been investigated for multi-view medical exams, particularly in the context of mammography.

We evaluate the effectiveness of our approach on two publicly available benchmark datasets of mammography images, namely CBIS-DDSM [39] and INbreast [2]. We conduct a meticulous experimental evaluation that demonstrates how our proposed models, owing to the aforementioned abilities, possess the means for properly leveraging information contained in multiple mammographic views and thus exceed the performance of both real-valued baselines and state-of-the-art methods. Finally, we further validate the proposed method on two additional benchmark datasets, i.e., Chexpert [40] for chest X-rays and BraTS19 [41], [42] for brain MRI, to prove the generalizability of the proposed approach in different

applications and medical exams, going beyond mammograms and classification.

The rest of the paper is organized as follows. Section II gives a detailed overview of the multi-view approach for breast cancer analysis, delving into why it is important to design a painstaking multi-view method. Section III provides theoretical aspects and concepts of hypercomplex models, and Section IV presents the proposed method. The experiments are set up in Section V and evaluated in Section VI. A summary of the proposed models with specific data cases is provided in Section VIII, while conclusions are drawn in Section IX.

II. MULTI-VIEW APPROACH IN BREAST CANCER ANALYSIS

There exist several types of medical exams for the detection process of breast cancer, such as mammography, ultrasound, biopsy, and so on. Among these, mammography is considered the best imaging method for breast cancer screening and the most effective for early detection [3]. A mammography exam comprises four X-ray images produced by the recording of two views for each breast: the CC view, which is a top to bottom view, and the MLO view, which is a side view. The diagnosis procedure adopted by radiologists consists in looking for specific abnormalities, the most common being masses, calcifications, architectural distortions of breast tissue, and asymmetries [2]. During the reading of a mammography exam, employing multiple views is crucial in order to make an accurate diagnosis, as they retain highly correlated characteristics, which, in reality, represent complementary information. Admittedly, comparing ipsilateral views (CC and MLO views of the same breast) helps to detect eventual tumors, as sometimes they are visible only in one of the two views, and additionally helps to analyze the 3D structure of masses. Whereas, studying bilateral views (same view of both breasts) helps to locate masses as asymmetries between them are an indicating factor [5]. An example of a complete mammogram exam with ipsilateral and bilateral views is shown in Fig. 2.

Given the multi-view nature of the exam and the multi-view approach employed by radiologists, many works are focusing on utilizing two or four views for the purpose of classifying breast cancer, with the goal of leveraging the information coming from ipsilateral and/or bilateral views. Indeed, studies have shown that a model employing multiple views can learn to generalize better compared to its single-view counterpart, increasing its discriminative power, while also reducing the number of false positives and false negatives [6], [9], [18].

Several works show the advantages of leveraging multiple views by adopting simple approaches. For instance, one approach involves simply averaging the predictions generated by the same model when provided with two ipsilateral views [6], which can be classified as a late-fusion approach. However, late-fusion methods ignore local interactions between views [29]. In contrast to late-fusion, also early-fusion techniques have been employed. These techniques involve the concatenation of feature vectors into a single vector [43]. Nevertheless, the issue with early fusion is that it treats the resulting vector as a unimodal input, potentially failing to fully exploit

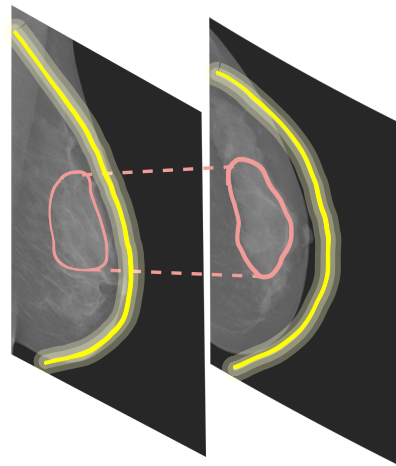


Fig. 3. Global and local relations. Global relations are intra-view features, e.g., the shape of the breast (depicted in shades of yellow). Local relations are inter-view features, e.g., textures (depicted in red).

the complementary nature of the views [44], [45]. Instead, more complex approaches consist in designing multi-view architectures that exploit correlations for learning and not just at inference time, like late-fusion methods. Recent techniques such as these propose architectures comprising multiple convolutional neural networks (CNNs) paths or *columns*, where each column processes a different view and their output is subsequently concatenated together and fed to a number of fully connected layers to obtain the final output [18]–[25]. A recent paper proposes an approach to utilize the complete mammography exam, thus comprised of four views [18]. Alternatively, a number of works [20]–[22], [26] adopt the same idea of having multiple columns but instead focus on using just two ipsilateral views.

Even though multimodal methods have been employed in a variety of recent deep learning works for breast cancer analysis, not much attention has been paid to how the DL model actually leverages information contained in the multiple views. Indeed, a recent study shows that such multimodal approaches might actually fail to exploit such information, leading to a counter-intuitive situation in which the single-view counterpart outperforms the multi-view one [19]. Therefore, just employing an architecture with multiple columns for each view is not enough to really leverage the knowledge coming from the correlated inputs [19]. Even in other applications of multimodal learning (e.g., involving speech or text), it is a common phenomenon that DL networks that are not properly modeled, fail to utilize the information contained in the different input modalities [30]. Although the context may differ, this underlying issue is a common concern in the multimodal and multi-view scenarios. Therefore, when processing multi-view exams, a painstaking and meticulous method has to be developed. To this end, we propose a method based on hypercomplex algebra, whose properties are described in the following sections.

III. QUATERNION AND HYPERCOMPLEX NEURAL NETWORKS

Quaternion and hypercomplex neural networks have their foundations in a hypercomplex number system \mathbb{H} equipped with its own algebra rules to regulate additions and multiplications. Hypercomplex numbers generalize a plethora of algebraic systems, including complex numbers \mathbb{C} , quaternions \mathbb{Q} and octonions \mathbb{O} , among others. A generic hypercomplex number is defined as

$$h = h_0 + h_1\hat{i}_1 + \dots + h_i\hat{i}_i + \dots + h_{n-1}\hat{i}_{n-1}, \quad (1)$$

whereby h_0, \dots, h_{n-1} are the real-valued coefficients and $\hat{i}_1, \dots, \hat{i}_{n-1}$ the imaginary units. The first coefficient h_0 represents the real component, while the remaining ones compose the imaginary part. Therefore, the algebraic subsets of \mathbb{H} are identified by the number of imaginary units and by the algebraic rules that govern the interactions among them. For instance, a complex number has just one imaginary unit, while a quaternion has three imaginary units. In the latter domain, the vector product is not commutative so the Hamilton product has been introduced to multiply two quaternions. Interestingly, a real number can be expressed through eq. (1) by setting $i = 0$ and considering the real part only. Being hypercomplex algebras part of the Cayley-Dickson algebras, they always have a dimension equal to a power of 2, therefore it is important to note that subset domains exist solely at pre-defined dimensions, i.e., $n = 2, 4, 8, 16, \dots$, while no algebra rules have been discovered yet for other values.

The addition operation is performed through an element-wise addition of terms, i.e., $h+p = (h_0+p_0) + (h_1+p_1) + \dots + (h_i+p_i)\hat{i}_i + \dots + (h_{n-1}+p_{n-1})\hat{i}_{n-1}$. Similarly, the product between a quaternion and a scalar value $\alpha \in \mathbb{R}$ can be formulated with $\alpha h = \alpha h_0 + \alpha h_1 + \dots + \alpha h_i\hat{i}_i + \dots + \alpha h_{n-1}\hat{i}_{n-1}$ by multiplying the scalar to real-valued components. Nevertheless, with the increasing of n , Cayley-Dickson algebras lose some properties regarding the vector multiplication, and more specific formulas need to be introduced to model this operation because of imaginary units interplays [46]. Indeed, as an example, quaternions and octonions products are not commutative due to imaginary unit properties for which $\hat{i}_1\hat{i}_2 \neq \hat{i}_2\hat{i}_1$. Therefore, quaternion convolutional neural network (QCNN) layers are based on the Hamilton product, which organizes the filter weight matrix to be encapsulated into a quaternion as $\mathbf{W} = \mathbf{W}_0 + \mathbf{W}_1\hat{i}_1 + \mathbf{W}_2\hat{i}_2 + \mathbf{W}_3\hat{i}_3$ and to perform convolution with the quaternion input $\mathbf{x} = \mathbf{x}_0 + \mathbf{x}_1\hat{i}_1 + \mathbf{x}_2\hat{i}_2 + \mathbf{x}_3\hat{i}_3$ as:

$$\mathbf{W} * \mathbf{x} = \begin{bmatrix} \mathbf{W}_0 & -\mathbf{W}_1 & -\mathbf{W}_2 & -\mathbf{W}_3 \\ \mathbf{W}_1 & \mathbf{W}_0 & -\mathbf{W}_3 & \mathbf{W}_2 \\ \mathbf{W}_2 & \mathbf{W}_3 & \mathbf{W}_0 & -\mathbf{W}_1 \\ \mathbf{W}_3 & -\mathbf{W}_2 & \mathbf{W}_1 & \mathbf{W}_0 \end{bmatrix} * \begin{bmatrix} \mathbf{x}_0 \\ \mathbf{x}_1 \\ \mathbf{x}_2 \\ \mathbf{x}_3 \end{bmatrix}. \quad (2)$$

Processing multidimensional inputs with QCNNs has several advantages. Indeed, due to the reusing of filter submatrices \mathbf{W}_i , $i = 0, \dots, 3$ in eq. (2), QCNNs are defined with 1/4 free parameters with respect to real-valued counterparts with the same architecture structure. Moreover, sharing the filter submatrices among input components allows QCNNs to

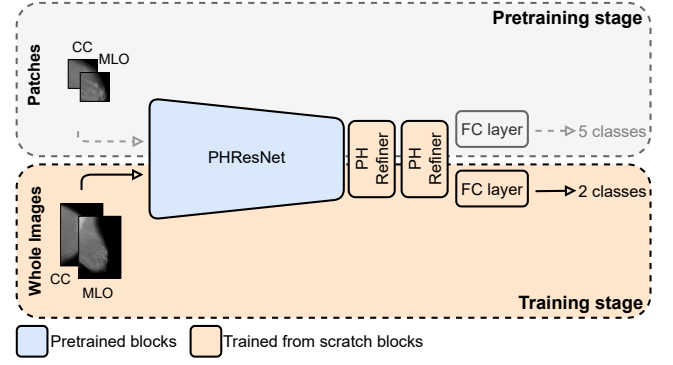


Fig. 4. Training pipeline and PHResNet overview. We employ a pretraining stage to overcome issues presented in Section `efsubsec:training`. During this stage, the PHResNet is trained on patches extracted from the original mammogram. They are classified into five classes: background or normal, benign and malignant calcifications and masses, respectively. At downstream time, i.e., when training on whole images, two PH convolutional refiner blocks are added and trained from scratch together with the final classification layer.

capture internal relations in input dimensions and to preserve correlations among them [32], [47]. However, this approach is limited to 4D inputs, thus various knacks are usually employed to apply QCNNs to different 3D inputs, such as RGB color images. In these cases, a padding channel is concatenated to the three-channel image to build a 4D image adding, however, useless information. Similarly, when processing grayscale images with QCNNs, the single channel has to be replicated in order to be fed into the quaternion-valued network, without annexing any additional information for the model. Recently, novel approaches proposed to parameterize hypercomplex multiplications and convolutions to maintain QCNNs and hypercomplex algebras advantages, while extending their applicability to any n D input [37], [38]. The core idea of these methods is to develop the filter matrix \mathbf{W} as a parameterized sum of Kronecker products:

$$\mathbf{W} = \sum_{i=0}^n \mathbf{A}_i \otimes \mathbf{F}_i, \quad (3)$$

whereby n is a tunable or user-defined hyperparameter that determines the domain in which the model operates (i.e., $n = 4$ for the quaternion domain, $n = 8$ for octonions, and so on). The matrices \mathbf{A}_i encode the algebra rules, that is the filter organization for convolutional layers, while the matrices \mathbf{F}_i enclose the weight filters. Both these elements are completely learned from data during training, thus grasping algebra rules or adapting them, if no algebra exists for the specific value of n , directly from inputs. The PHC layer is malleable to operate in any n D domain by easily setting the hyperparameter n , thus extending QCNNs advantages to every multidimensional input. Indeed, PHNNs can process color images in their natural domain ($n = 3$) without adding any uninformative channel (as previously done for QCNNs), while still exploiting latent relations between channels. Moreover, due to the data-driven fashion in which this approach operates, PHNNs with $n = 4$ outperform QCNNs both in terms of prediction accuracy and training as well as inference time [37], [38]. Furthermore, PHC

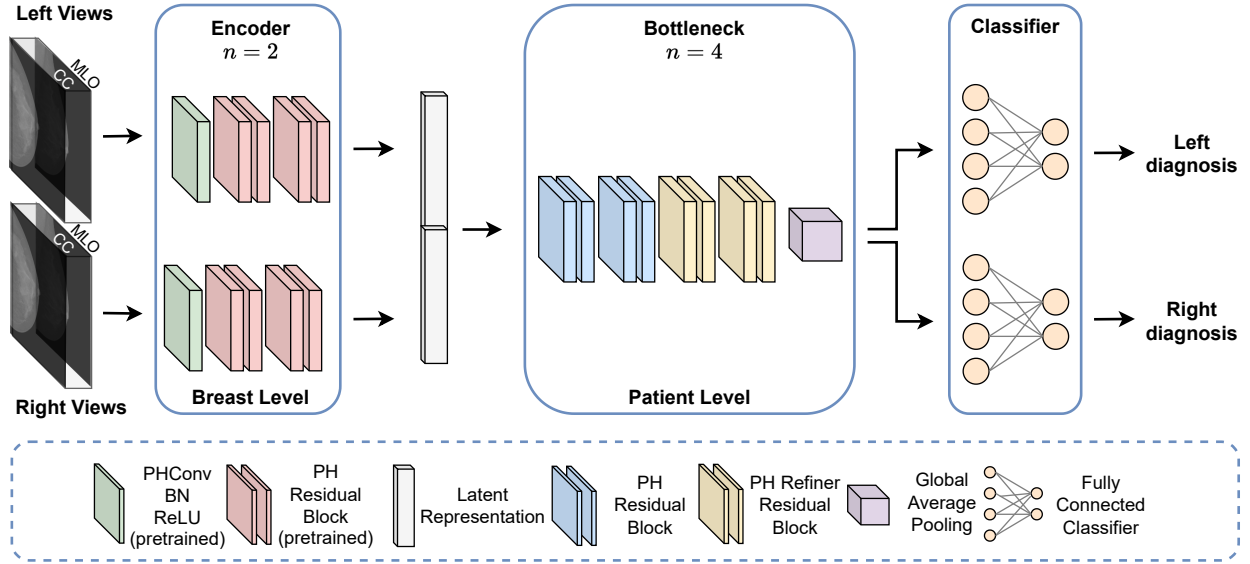


Fig. 5. PHYBONet architecture. The model first performs a breast-level analysis by taking as input two pairs of ipsilateral views that are handled by two pretrained PH encoder branches with $n = 2$. The learned latent representations are then processed in a joint fashion by four PH residual blocks with $n = 4$. Finally, the outputs from the two branches are fed to a separate final fully connected layer after a global average pooling operation.

layers employ $1/n$ free parameters with respect to real-valued counterparts, so the user can govern both the domain and the parameters reduction by simply setting the value of n .

The reason behind the success of hypercomplex models is their ability to model not only global relations as standard neural networks but also local relations. Global dependencies are related to spatial relations among pixels of the same level (i.e., for an RGB image, the R, G, and B channels are different levels). Instead, local dependencies implicitly link different levels. In the latter case, implicit local relations for an RGB image are the natural link that exists within the three-channel components defining a pixel. This kind of correlation among the different levels of the input is usually not taken into account by conventional neural networks that operate in the real domain, as they consider the pixels at different levels as sets of decorrelated points [32]. Considering the multiple dimensions/levels of a sample as unrelated components may break the inner nature of the data, losing information about the inner structure of the sample. Instead, PHNNs can explore both global and local relations, not losing crucial information. Indeed, global relations are modeled as in conventional models, e.g., with convolutional operations. Rather, thanks to the formulation of convolution defined in Eq. 2, the filter submatrices are shared among input dimensions, i.e., the different levels, thus hypercomplex networks are endowed with the ability to model also local relations. In the context of mammography, the different views can be regarded as the color channels of an RGB image. Thus, global relations are intra-view features, such as the shape of the breast. In contrast, local relations are inter-view features, thus encompassing the interdependencies found across the various views. A depiction of such relations in the context of a mammography exam can be seen in Fig. 3. Indeed, local relations are an inherent part of multi-view data. Nevertheless, standard neural networks

have been shown to ignore such relations [32]. Therefore, hypercomplex algebra may be a powerful tool to leverage mammogram views as it is able to describe multidimensional data preserving its inner structure [38].

IV. PROPOSED METHOD

In the following section, we expound the proposed approach and we delineate the structure of our models and the training recipes we adopt. More in detail, we design *ad hoc* networks for two-view and four-view exams, i.e., a complete mammography exam.

A. Multi-view PHResNet

The core idea of our method is to take advantage of the information contained in multiple views through PHC layers in order to obtain a more performant and robust classifier for breast cancer.

ResNets are among the most widespread models for medical image classification [6], [9], [15], [18], [19], [48], [49]. They are characterized by residual connections that ensure proper gradient propagation during training. A ResNet block is typically defined by:

$$\mathbf{y} = \mathcal{F}(\mathbf{x}) + \mathbf{x}, \quad (4)$$

where $\mathcal{F}(\mathbf{x})$ is usually composed by interleaving convolutional layers, batch normalization (BN) and ReLU activation functions. When equipped with PHC layers, real-valued convolutions are replaced with PHC to build PHResNets, therefore $\mathcal{F}(\mathbf{x})$ becomes:

$$\mathcal{F}(\mathbf{x}) = \text{BN}(\text{PHC}(\text{ReLU}(\text{BN}(\text{PHC}(\mathbf{x}))))), \quad (5)$$

in which \mathbf{x} can be any multidimensional input with correlated components. It is worth noting that PH models generalize real-valued counterparts and also monodimensional inputs. As a

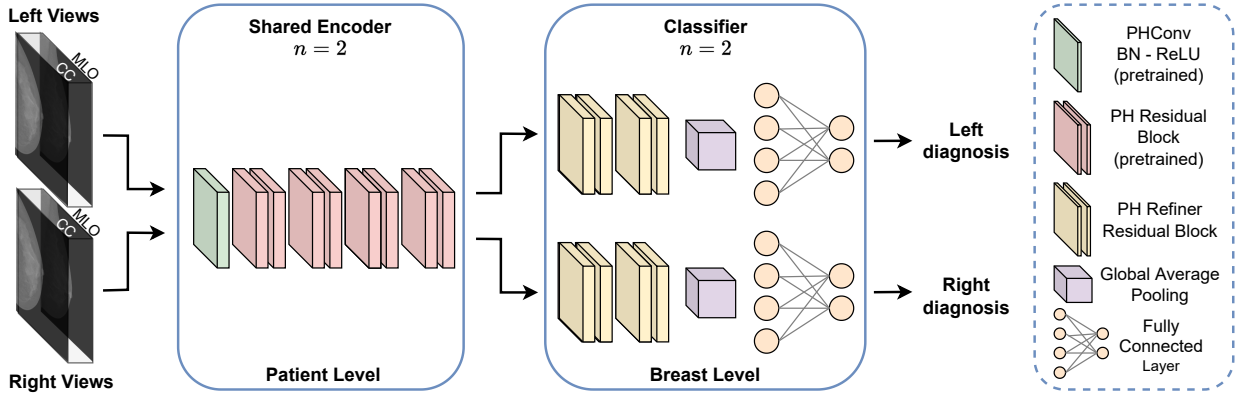


Fig. 6. PHYSEnet architecture. The model comprises an initial deep patient-level framework that takes as input two pairs of ipsilateral views which are processed by a pretrained shared PHResNet18 with $n = 2$ that serves as the encoder. Ultimately, the two learned latent representations are fed to the respective classification branch composed of PH refiner residual blocks with global average pooling and the final fully connected layer to perform the breast-level learning.

matter of fact, a PH model with $n = 1$ is equivalent to a real-valued model receiving 1D inputs.

B. PH architectures for two views

The proposed multi-view architecture in the case of two views is straightforward. We employ PHResNets and we fix the hyperparameter $n = 2$. The model is depicted in Fig. 4 together with the training strategy we deploy. The two views of the same breast, i.e., ipsilateral views, are fed to the network as a multidimensional input (channel-wise) enabling PHC layers to exploit their correlations. We adopt ipsilateral views because, as mentioned in Section VI-B, they help in both the detection and classification process, unlike bilateral views which aid only in the former.

Ultimately, the model produces a binary prediction indicating the presence of either a malignant or benign/normal finding (depending on the dataset). In such a manner, the model is able to process the two mammograms as a unique entity by preserving the original multidimensional structure as elucidated in Section III [32]. As a consequence, it is endowed with the capacity to exploit both global and local relations, i.e., the interactions between the highly correlated views, mimicking the diagnostic process of radiologists.

C. PH architectures for four views

1) *PHYBOnet*: The first model we propose is shown in Fig. 5, namely Parameterized Hypercomplex Bottleneck network (PHYBOnet). PHYBOnet is based on an initial breast-level focus and a consequent patient-level one, through the following components: two encoder branches for each breast side with $n = 2$, a bottleneck with the hyperparameter $n = 4$ and two final classifier layers that produce the binary prediction relative to the corresponding side. Each encoder takes as input two views (CC and MLO) and has the objective of learning a latent representation of the ipsilateral views. The learned latent representations are then merged together and processed by the bottleneck which has n set to 4 in order for PHC layers to grasp correlations among them. Indeed, in this way we additionally obtain a light network since the number of parameters is reduced by $1/4$.

2) *PHYSEnet*: The second architecture we present, namely Parameterized Hypercomplex Shared Encoder network (PHYSEnet), is depicted in Fig. 6. It has a broader focus on the patient-level analysis through an entire PHResNet18 with $n = 2$ as the encoder model, which takes as input two ipsilateral views. The weights of the encoder are shared between left and right inputs to jointly analyze the whole information of the patient. Then, two final classification branches, consisting of residual blocks and a final fully connected layer, perform a breast-level analysis to output the final prediction for each breast. This design allows the model to leverage information from both ipsilateral and bilateral views. Indeed, thanks to PHC layers, ipsilateral information is leveraged as in the case of two views, while by sharing the encoder between the two sides, the model is also able to take advantage of bilateral information.

D. Training procedure

Training a classifier from scratch for this kind of task is very difficult for a number of reasons. To begin, neural models require huge volumes of data for training, but there are only a handful of publicly available datasets for breast cancer, which also present a limited number of examples. Additionally, a lesion occupies only a tremendously small portion of the original image, thus making it arduous to be detected by a model [6].

To overcome these challenges, we deploy an *ad hoc* pre-training strategy, illustrated in Fig. 4 divided into two main steps. First, we pretrain the model on patches of mammograms and, second, we involve the pretrained weights to initialize the network for training on whole images. Specifically, in the first step patches are extracted from the original mammograms by taking 20 patches for each lesion present in the dataset: 10 of background or normal tissue and 10 around the region of interest (ROI) in question. Aiming to utilize this classifier for the training of whole mammograms with two views, we also require two views at the patch level. The definition of two views for patches is straightforward. For all lesions that are visible in both views of the breast, patches around that lesion

are taken for both views. Thus, the patch classifier takes as input two-view 224×224 patches of the original mammogram, concatenated along the channel dimension and classifies them into one of the following five classes: extitbackground or normal, benign calcification, malignant calcification, benign mass, and malignant mass [6]. At downstream time, i.e., when training on whole images, the network is initialized with the pretrained weights to classify exams as either malignant or benign. Indeed, pretraining on patches is a way to exploit the fine-grained detail characteristic of mammograms which is crucial for discriminating between malignant and benign findings, that would otherwise be lost due to the resizing of images [6], [18]. Such training strategy plays a determining role in boosting the performance of the models as we demonstrate in the experimental Section VI.

V. EXPERIMENTAL SETUP

In this section, we describe the experimental setup of our work that comprises the datasets we consider, the metrics employed for evaluation, model architectures details and training hyperparameters.

A. Data

We validate the proposed method with two publicly available datasets of mammography images, whose sample summary is presented in Tab. I. We additionally demonstrate the generalizability and flexibility of the proposed method on two additional tasks and datasets described herein.

1) *CBIS-DDSM*: The Curated Breast Imaging Subset of DDSM (CBIS-DDSM) [39] is an updated and standardized version of the Digital Database for Screening Mammography (DDSM). It contains 2478 scanned film mammography images in the standard DICOM format and provides both pixel-level and whole-image labels from biopsy-proven pathology results. Furthermore, for each lesion, the type of abnormality is reported: calcification (753 cases) or mass (891 cases). Importantly, the dataset does not contain healthy cases but only positive ones (i.e., benign or malignant), where for the majority of them a biopsy was requested by the radiologist in order to make a final diagnosis, meaning that the dataset is mainly comprised of the most difficult cases. Additionally, the dataset provides the data divided into splits containing only masses and only calcifications, respectively, in turn split into official training and test sets, characterized by the same level of difficulty. CBIS-DDSM is employed for the training of the patch classifier as well as whole-image classifier in the two-view scenario. It is not used for four-view experiments as the official training/test splits do not contain enough full-exam cases and creating different splits would result in data leakage between patches and whole images. Finally, the images are resized to 600×500 and are augmented with a random rotation between -25 and $+25$ degrees and a random horizontal and vertical flip [6], [8].

2) *INbreast*: The second dataset employed in this study, INbreast [2], is a database of full-field digital mammography (FFDM) images. It contains 115 mammography exams for a total of 410 images, involving several types of lesions,

TABLE I
DATA DISTRIBUTION FOR SPLITS OF CBIS-DDSM AND FOR INBREAST WHEN CONSIDERING TWO AND FOUR VIEWS. IN THE WHOLE TABLE, TWO VIEWS OF THE SAME BREAST ARE COUNTED AS ONE INSTANCE.

CBIS-DDSM				
	Mass split		Mass-calc split	
	Malignant	Benign	Malignant	Benign/Normal
Train	254	255	480	582
Test	59	83	104	149
INbreast				
	Two views		Four views	
	Malignant	Benign	Malignant	Benign/Normal
Train	34	89	33	85
Test	14	39	8	22

among which are masses and calcifications. The data splits are not provided, thus they are manually created by splitting the dataset patient-wise in a stratified fashion, using 20% of the data for testing. Finally, INbreast does not provide pathological confirmation of malignancy but BI-RADS labels. Therefore, in the aim of obtaining binary labels, we consider BI-RADS categories 4, 5 and 6 as positive and 1, 2 as negative, whilst ruling out category 3 following the approach of [6]. INbreast is utilized for experiments in both the two-view and four-view scenarios and the same preprocessing as CBIS-DDSM is applied. Finally, as can be seen in Tab. I, the dataset is highly imbalanced. To tackle this issue, in addition to using the same data augmentation techniques employed for CBIS-DDSM, we deploy a weighted loss during training, as elaborated in Section V-C.

3) *CheXpert*: The CheXpert [40] dataset contains 224,316 chest X-rays with both frontal and lateral views and provides labels corresponding to 14 common chest radiographic observations. Images are resized to 320×320 [40] for training and the same augmentation operations as before are applied.

4) *BraTS19*: BraTS19 [41], [42], [50] is a dataset of multimodal brain MRI scans, providing four modalities for each exam, segmentation maps, demographic information (such as age) and overall survival (OS) data as the number of days, for 210 patients. For training, volumes are resized to $128 \times 128 \times 128$ and augmented via random scaling between 1 and 1.1 [51] for the task of overall survival prediction. Rather, for segmentation, 2D axial slices are extracted from the volumes and the original shape of 240×240 is maintained.

B. Evaluation metrics

We adopt AUC (Area Under the ROC Curve) as the main performance metric to evaluate our models, as it is one of the most common metrics employed in medical imaging tasks [6], [18]–[20]. The ROC curve summarizes the trade-off between True Positive Rate (TPR) and False Positive Rate (FPR) for a predictive model using different probability thresholds. To further assess network performance, we additionally evaluate our models in terms of classification accuracy. Finally, we employ the Dice score for the segmentation task, which

measures the pixel-wise agreement between a predicted mask and its corresponding ground truth.

C. Training details

We train our models to minimize the binary cross-entropy loss using Adam optimizer [52], with a learning rate of 10^{-5} for classification experiments and 2×10^{-4} for segmentation. Regarding two-view models, the batch size is 8 for PHResNet18, 2 for PHResNet50 and 32 for PHUNet. Instead, for four-view models the batch size is set to 4. Notably, in our initial experiments concerning four-view exams, we employed a standard cross-entropy loss. However, the models struggled to generalize due to the high class imbalance within the dataset. Consequently, to address this issue and achieve meaningful results, we adopted a weighted loss [53], [54] assigning a weight to positive examples equal to the number of benign/normal examples divided by the number of positive examples. We adopt two regularization techniques: weight decay at 5×10^{-4} and early stopping.

1) *Two-view architectures*: We perform the experimental validation with two ResNet backbones: PHResNet18 and PHResNet50. The networks have the same structure as in the original paper [38] with some variations. In the first convolutional layer, the number of channels in input is set to be equal to the hyperparameter $n = 2$ and we omit the max pooling operation since we apply a global average pooling operation, after which we add 4 refiner residual blocks constructed with the bottleneck design [55]. Ultimately, the output of such blocks is fed to the final fully connected layer responsible for classification. The backbone network is initialized with the patch classifier weights, while the refiner blocks and final layer are trained from scratch, following the approach of [6]. In both hypercomplex and real domains, the models take as input two views as if they were a single multi-dimensional (channel-wise) entity.

2) *Four-view architectures*: Here, we expound the architectural details of the proposed models when considering as input the whole mammogram exam. Also in this case, we use as baselines the respective real-valued counterparts, the bottleneck model (BOnet) and the shared encoder network (SEnet), for which the structural details are the same as in the hypercomplex domain.

The first proposed model is PHYBOnet. We start from a PHResNet18 and divide its blocks such that the first part of the network serves as an encoder for each side and the remaining blocks compose the bottleneck. Thus, the encoders comprise a first 3×3 convolutional layer with a stride of 1, together with batch normalization and ReLU, and the first 4 residual blocks of ResNet18, as shown in Fig. 5. Then, the bottleneck is composed of 8 residual blocks and a global average pooling layer, with the first 4 residual blocks being the standard remaining blocks of ResNet18, and the last 4 the refiner residual blocks employed also in the architecture with two views. Finally, the two outputs are fed to the respective fully connected layer, each responsible to produce the prediction related to its side. The second proposed architecture, PHYSEnet, presents as shared encoder model a whole PHResNet18, while the

TABLE II
RESULTS FOR PATCH CLASSIFIERS ON CBIS DATASET CONTAINING BOTH MASS AND CALC. THE PHRESNETS OUTPERFORM REAL-VALUED COUNTERPARTS.

Model	Accuracy (%)
ResNet18	74.942
PHResNet18	76.825
ResNet50	75.989
PHResNet50	77.338

two classifier branches are comprised of the 4 refiner blocks with a global average pooling layer and the final classification layer. For both proposed models, the choice of PHResNet18 as backbone instead of PHResNet50 is motivated by the results obtained in the experimental evaluation in the two-view scenario described in Subsection VI-B2.

At training time, both for PHYBOnet and PHYSEnet, the encoder portions of the networks are initialized with the patch classifier weights, while the rest is trained from scratch. Rather, in a second set of experiments conducted only with PHYSEnet, the whole architecture is initialized with the weights of the best whole-image two-view classifier trained on CBIS-DDSM.

VI. EXPERIMENTAL EVALUATION

In this section, we present an exhaustive evaluation of our method, firstly investigating preliminary experiments without pretraining and then in detail with two multi-view scenarios. We validate our proposed framework by comparing it against real-valued counterparts and state-of-the-art models for multi-view breast cancer classification. Finally, we show the efficacy and the generalizability of the proposed architectures by going beyond breast cancer, considering two additional medical problems regarding multi-view chest X-rays and multimodal brain MRIs. For all experiments, the mean AUC and accuracy over multiple runs are reported together with the standard deviation.

A. Preliminary experiments

1) *Whole-image without pretraining*: We conduct preliminary experiments to evaluate the ability of the models to learn from data without any form of pretraining (first part of Tab. III). We test four different architectures on whole mammograms of CBIS-DDSM considering the mass data split. We employ PHResNet18 and PHResNet50 compared against their real-valued counterparts ResNet18 and ResNet50, respectively. Herein, it is evident that all the models involved are not able to learn properly and struggle to discriminate between images containing a benign lesion from images containing a malignant lesion. In fact, distinguishing the malignancy of an abnormality from the whole image only is extremely challenging because the lesion itself occupies a minuscule portion of the entire image. Nevertheless, even with poor performance, it is already evident that the proposed PHResNets are able to capture more information contained in the correlated views and thus reach a higher AUC and accuracy with respect to the

TABLE III

RESULTS FOR TWO-VIEW MODELS. FOR CBIS DATASET - MASS SPLIT, WE PERFORM EXPERIMENTS WITH NO PRETRAINING AND WITH PRETRAINING ON PATCHES. FOR CBIS DATASET - MASS AND CALC SPLIT, EXPERIMENTS ARE CONDUCTED WITH MODELS PRETRAINED ON PATCHES. FOR THE INBREAST DATASET, WE PRETRAIN THE MODELS ON PATCHES AND THEN ON WHOLE CBIS IMAGES (PATCHES + CBIS). RESULTS INDICATED IN BOLD AND UNDERLINED TEXT REPRESENT THE BEST AND SECOND-BEST OUTCOMES. OUR METHODS EXCEED REAL-VALUED BASELINES AND STATE-OF-THE-ART MODELS IN EACH TEST WE CONDUCT.

Dataset	Model	Params	Pretraining	AUC	Accuracy (%)
CBIS (mass)	ResNet18	11M	X	0.646 ± 0.008	64.554 ± 2.846
	ResNet50	16M		0.663 ± 0.011	67.606 ± 1.408
	PHResNet18 (ours)	5M		0.660 ± 0.020	67.371 ± 2.846
	PHResNet50 (ours)	8M		0.700 ± 0.002	70.657 ± 1.466
CBIS (mass)	ResNet18	26M	Patches	0.710 ± 0.018	70.892 ± 3.614
	ResNet50	32M		0.724 ± 0.007	73.474 ± 1.076
	Shared ResNet [19]	12M		0.735 ± 0.014	72.769 ± 2.151
	Breast-wise-model [18]	23M		0.705 ± 0.011	69.484 ± 2.151
	DualNet [56]	13M		0.705 ± 0.018	69.719 ± 1.863
	PHResNet18 (ours)	13M		<u>0.737 ± 0.004</u>	<u>74.882 ± 1.466</u>
	PHResNet50 (ours)	16M		0.739 ± 0.004	75.352 ± 1.409
CBIS (mass and calc)	ResNet18	26M	Patches	0.659 ± 0.012	66.271 ± 1.271
	ResNet50	32M		0.659 ± 0.013	65.217 ± 3.236
	PHResNet18 (ours)	13M		0.677 ± 0.005	68.116 ± 1.388
	PHResNet50 (ours)	16M		0.676 ± 0.014	<u>67.062 ± 0.995</u>
INbreast	ResNet18	26M	Patches + CBIS	0.789 ± 0.073	81.887 ± 1.509
	ResNet50	32M		0.755 ± 0.063	77.358 ± 7.825
	PHResNet18 (ours)	13M		0.793 ± 0.071	83.019 ± 5.723
	PHResNet50 (ours)	16M		0.759 ± 0.045	80.000 ± 6.382

real-valued models in all the experiments. Indeed, the best-performing model, i.e., the PHResNet50, achieves an AUC of 0.70 and accuracy of 70.657%. Although the networks reach good results considering the limited number of examples for training, to overcome the challenge of learning from whole mammograms, all further experiments exploit the pretraining strategy described in Subsection IV-D.

2) *Patch classifier*: Preliminary experiments also include the pretraining phase of patch classifiers, which is carried out with the purpose of overcoming the problems described in Subsection IV-D and extracting crucial information concerning the lesions. Table II reports the results of these experiments. We can observe that at the patch level, there is a great gap in performance between our parameterized hypercomplex models and real ones, with PHResNet50 yielding 77.338% accuracy, further exhibiting the ability of PHC layers to leverage latent relations between multi-dimensional inputs.

B. Experiments with two views

1) *State-of-the-art methods for comparison*: We first compare the proposed PHResNets against the respective real-valued baseline models (ResNet18 and ResNet50) and thereafter against three state-of-the-art multi-view architectures [18], [19], [56]. The model proposed in [56] processes frontal and lateral chest X-rays, employing as backbone DenseNet121, while methods proposed in [18], [19] are designed for mammography images. To ensure a fair comparison with our own networks, new runs were conducted for these models, following the same experimental setup, data, and pretraining technique as employed for our models. Additionally, original architectures proposed in [18], [19] employ as backbone a variation of the standard ResNet50, namely ResNet22, which was designed specifically for the purpose

of handling high-resolution images. However, in our case the mammograms are resized as explained in Subsection V-A, thus we straightforwardly use the more proper ResNet18 instead. Finally, since [18] proposes networks designed to handle four views, to compare this approach with ours, we employ the proposed breast-wise-model by trivially considering only *half* of it: instead of having four ResNet columns (one per each view and side) we consider only two columns for the CC and MLO views of one side only.

2) *Results*: The results of the experiments we conduct in the two-view scenario are reported in Tab. III, together with the number of parameters for each model we train.

Firstly, the advantages of the employed pretraining strategy are clear by comparing the results in the top part of the table with the part corresponding to the pretraining on patches. Most importantly, the center of the table reveals that PHResNets clearly outperform both baseline counterparts implemented in the real domain and all other state-of-the-art methods, with PHResNet50 yielding 0.739 AUC and 75.352% accuracy in the mass split. Our approach achieves the best results also for the mass and calc splits. Although the overall performance is reduced in this case, it is expected since calcifications are harder to classify and, in fact, most works in the literature focus only on mass detection/classification [5], [13], [14], [27], [28]. In this case, PHResNet18 performs better than PHResNet50, which might be due to PHResNet50 resulting over-parameterized for the dataset. In fact, the latter achieves in general similar results to smaller PHResNet18, even in the case of the mass split. Nonetheless, in both data splits, the two highest AUC and accuracy values are obtained by the two PHResNets, demonstrating the advantages of our approach. On top of that, it is interesting to notice how our proposed models present the lowest standard deviation on AUC and accuracy

TABLE IV
RESULTS FOR FOUR-VIEW MODELS ON INBREAST. WE PRETRAIN MODELS ON CBIS PATCHES AS WELL AS PATCHES AND THEN WHOLE CBIS IMAGES FOR FURTHER FINE-TUNING. RESULTS INDICATED IN BOLD AND UNDERLINED TEXT REPRESENT THE BEST AND SECOND-BEST OUTCOMES.

Model	Params	Pretraining	AUC	Accuracy (%)
BOnet concat	27M		0.756 ± 0.047	70.000 ± 4.216
SEnet	41M		0.786 ± 0.090	73.333 ± 12.824
View-wise-model [18]	24M	Patches	0.768 ± 0.072	<u>75.333 ± 6.182</u>
Breast-wise-model [18]	24M		0.734 ± 0.027	72.667 ± 7.717
PHYBOnet (ours)	7M		0.764 ± 0.061	70.000 ± 7.601
PHYSEnet (ours)	20M		0.798 ± 0.071	77.333 ± 7.717
SEnet	41M		Patches + CBIS	0.796 ± 0.096
PHYSEnet (ours)	20M	0.814 ± 0.060		82.000 ± 6.864

over different runs, which may indicate less sensibility to initialization and generally more robustness. Moreover, we have also conducted statistical significance tests to further validate our results. For example, in the case of mass classification with pretraining, the p -value between PHResNet18 and ResNet18 is 0.057, while between PHResNet50 and ResNet50 is 0.022, which are both statistically significant for a significance level of 0.10. Ultimately, compared with the baseline real-valued networks, PHC-based models possess half the number of free parameters and, even so, are still able to outperform them, further proving how the hypercomplex approach truly takes advantage of the correlations found in mammogram views.

Then, an additional set of experiments is conducted with the INbreast dataset to further validate the proposed method. In this case, the models are initialized with the weights of the best whole-image classifier trained with CBIS-DDSM. Despite INbreast containing a very limited number of images, the features learned on CBIS-DDSM are transferred effectively so that the models are able to attain even better performance, i.e., an AUC of 0.793 and 83.019% accuracy obtained by PHResNet18. Also in this case, both PHResNets exceed the respective real-valued baselines and reduce the standard deviation, proving once more the generalizability of the networks and the ability of PHC layers to draw on the relations of mammographic views to achieve more accurate predictions.

Moreover, we can also observe that, throughout all the experiments with pretraining, the performance of PHResNet18 and PHResNet50 is comparable. The reason for this may be that PHResNet50 might result overparameterized for the relatively small datasets employed. For this reason, for four-view architectures we adopt PHResNet18 instead of PHResNet50 as the backbone, also considering the fact that the subset of complete exams further reduces the number of examples.

To conclude, experiments presented in Tab. III serve also as an ablation study. In fact, the main component of the networks that we propose are PHC layers and by removing them the models turn out to be equivalent to their real-valued counterparts, which we have thoroughly tested in each scenario.

C. Experiments with four views

1) *State-of-the-art methods for comparison:* We first compare the proposed architectures against the respective baseline models implemented in the real domain (BOnet and SEnet),

and further against two state-of-the-art approaches designed for breast cancer [18]. Specifically, we employ as comparison their best-performing model, the view-wise-model, along with the breast-wise-model, since we already consider it for the case of two views. The same considerations mentioned in Subsection VI-B1 apply herein as well: ResNet22 is replaced with ResNet18, and new runs are conducted with the same dataset and pretraining procedure as our models to guarantee a fair comparison.

2) *Results:* In Tab. IV, we can observe the number of free parameters for each model and the results on the INbreast dataset with four views. Since this is a small dataset, in order to avoid overfitting, we perform cross-validation considering 5 different splits.

The proposed PH models reach higher accuracy and AUC with respect to the equivalent real-valued baselines, achieving so with half/a quarter of the number of free parameters, thus highlighting the role that correlations between mammographic views play in making the right prediction if exploited properly, as our hypercomplex models are able to do. Importantly, our PHYSEnet largely outperforms all other models, attaining an AUC of 0.798 and accuracy of 77.333%, proving how the simultaneous exploitation of ipsilateral views, related to PHC layers, and the shared weights between bilateral views of the encoder model results in a more performing classifier. Indeed, PHYSEnet has an initial deep patient-level block that encodes view embeddings by sharing weights between the two sides, providing a more powerful representation with respect to the ones given by the breast-level encoders of PHYBOnet. Interestingly, our second proposed network, PHYBOnet with $n = 4$, is also able to compete with the best models in the state-of-the-art, surpassing the breast-wise model and having overall comparable performance with only 7M parameters. Furthermore, we have performed statistical significance tests to corroborate our findings. For example, the p -value between PHYSEnet and the state-of-the-art Breast-wise-model is 0.076 which is statistically significant for a significance level of 0.10.

Ultimately, we also test the most performing architecture, that is PHYSEnet, together with its equivalent implemented in the real domain, using as initialization the weights of the best whole-image two-view model trained with CBIS-DDSM. Both models benefit from the learned features on whole images instead of patches, gaining a boost in performance. However, the greater improvement is attained by the PHC version of the network, which once again surpasses the performance of

all other experiments with an AUC of 0.814 and accuracy of 82%.

In conclusion, by comparing our method against the respective real-valued models in Tab. IV, these experiments also serve as ablation studies, as explained in Section VI-B2.

D. Generalizing beyond mammograms

We conduct three additional sets of experiments to further validate the efficacy of the proposed method and its generalizability to different medical scenarios and on a finer-scaled task, i.e., segmentation.

1) *Multi-view multi-label chest X-ray classification*: The task consists in classifying the 14 most common chest diseases from multi-view X-rays. The evaluation is then conducted on a subset of five labels according to the original task [40]. Since the exam comprises two views, we employ a PHResNet with $n = 2$ and compare it against its real-valued counterpart. As shown in Tab. V, PHResNet outperforms the real-valued ResNet, achieving an AUC of 0.722. We additionally compare our approach with the single-view model that won the CheXpert challenge, i.e., DeepAUC [57], which directly trains their network to classify the five evaluation labels instead of the whole 14. Their model is a single-view architecture, and the best performance was achieved through an ensemble of networks. To ensure a fair comparison, we conduct a new run using a single model and compare it with our approach, i.e., PHDeepAUC with $n = 2$, which is a multi-view adaptation of DeepAUC operating in the hypercomplex domain. Additionally, we modify the original DeepAUC to handle multiple views for a more straightforward comparison with our method. As can be seen in Tab. V, PHDeepAUC yields the highest AUC of 0.867, outperforming the best model proposed in the original challenge. Moreover, it is noteworthy that the multi-view version of DeepAUC performs worse than the original single-view model. Indeed, as described in Section II, these types of networks tend to overfit on one of the two views and, because of this, it might occur that the single-view model surpasses its multi-view respective [19], as it happens in this example. This result further validates the efficacy of our multi-view approach based on hypercomplex algebra, which instead effectively exploits information from both views and thus outperforms both multi-view and single-view state-of-the-art DeepAUC.

Finally, these results prove the generalizability of the proposed method with respect to other types of medical exams. In other words, the ability of hypercomplex networks to learn a more effective representation of a multi-view exam remains consistent across different medical imaging scenarios, such as chest X-rays.

2) *Multimodal overall survival prediction*: For this set of experiments, we consider one of the official tasks of the BraTS19 challenge [50], which is the prediction of the overall survival (OS) in number of days for each patient. The task evaluation is done considering three different classes: short-term (less than 10 months), mid-term (between 10 and 15 months), and long-term (more than 15 months) survivors. For this task, we employ a PHResNet18 3D, thus defining 3D

TABLE V
RESULTS FOR MULTI-VIEW MULTI-LABEL CLASSIFICATION ON CHEXPART.

Model	Params	AUC
ResNet18	11M	0.645 \pm 0.164
PHResNet18	5M	0.722 \pm 0.184
DeepAUC (single-view) [57]	6M	<u>0.834</u> \pm 0.002
DeepAUC (multi-view)	6M	0.820 \pm 0.012
PHDeepAUC ($n=2$)	3M	0.867 \pm 0.009

TABLE VI
RESULTS FOR OS PREDICTION ON OFFICIAL VALIDATION DATASET OF BRA-TS19.

Model	Params	Accuracy
Post-hoc [51]	310K	0.414
PH Post-hoc ($n = 4$)	91K	<u>0.448</u>
ResNet18 3D	33M	0.414
PHResNet18 3D ($n = 2$)	16M	0.517

parameterized hypercomplex convolutions. Specifically, the input consists of two modalities, T2 and FLAIR, and the age parameter. The volumes are processed by the PHResNet18 3D for which we set $n = 2$, while the age input is handled by a linear layer. Then, the learned features of the MRIs and the age are summed together [51] and processed by two fully connected layers to produce the final output, i.e., the estimated number of survival days. We train this architecture and its real-valued respective, ResNet18 3D, with an MSE loss. Moreover, we compare our method against a state-of-the-art architecture, Post-hoc [51], for which we conduct a new run, and its counterpart in the hypercomplex domain, PH Post-hoc. They employ as input the volumes corresponding to all four modalities provided by BraTS19 and the age parameter. Thus, we set the hyperparameter $n = 4$ for the branch that processes the MRIs, and $n = 1$ for the PHM layer that handles the age input. All the models are evaluated through the official online evaluation platform of the challenge on the provided validation set and the results are reported in Tab. VI. Both hypercomplex networks surpass their respective real-valued counterparts, with PHResNet18 3D achieving the highest accuracy 0.517, surpassing the state-of-the-art approach in both real and hypercomplex domains. Importantly, PH Post-hoc, which comprises only 91K parameters, outperforms ResNet18 3D, which instead has 33M parameters, further highlighting the power of exploiting not only global relations, as standard neural networks, but also local relations, thanks to hypercomplex operations.

To conclude, the experiment results in Tab. VI prove the flexibility of the method with respect to a different task, i.e., regression, and medical exam, i.e., brain MRI, as the hypercomplex networks far exceed the respective models in the real domain. Finally, these results also show that the proposed architectures can not only learn good representations from different views, i.e., a different angle of the same subject, but also from multiple modalities, i.e., the same view but containing different information.

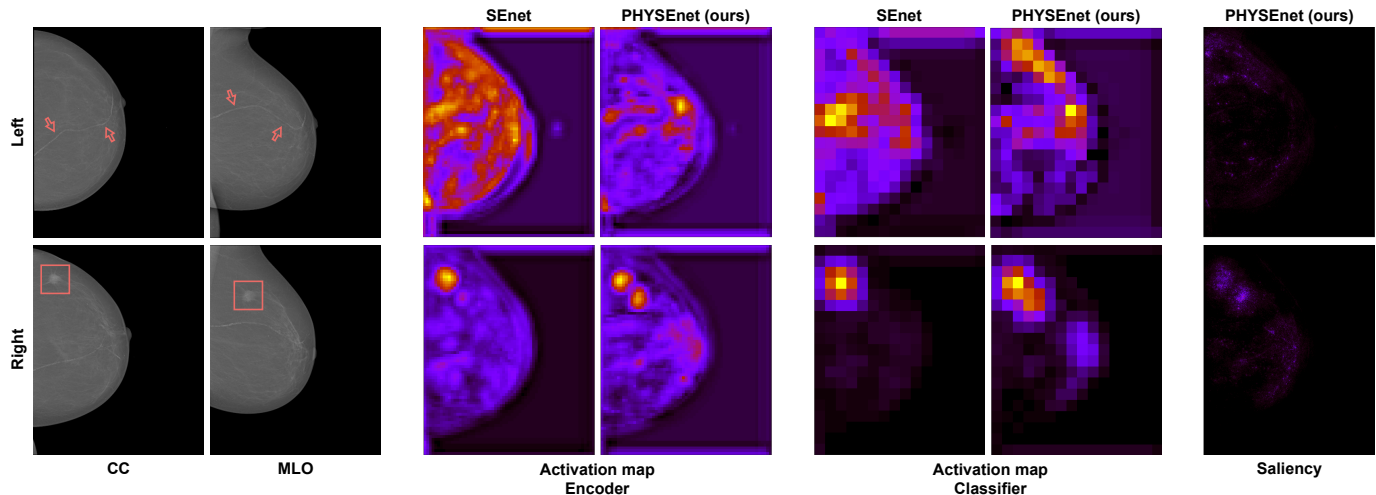


Fig. 7. From the left, a sample exam from the INbreast dataset containing a benign calcification on the left side and a malignant mass on the right side. Then, activation maps to visualize the learned latent representations of PHYSEnet and SEnet at encoder and classifier level. Lastly, the saliency map for PHYSEnet containing the most relevant pixels according to the gradient.

TABLE VII
RESULTS FOR BRAIN TUMOR SEGMENTATION ON BRATS19.

Model	Params	Dice Score
UNet	31M	0.826 \pm 0.017
PHUNet	15M	0.825 \pm 0.018

3) *Multimodal brain tumor segmentation*: Lastly, in this section, we demonstrate how this framework can easily be extended for different tasks and employed with any network architecture. To this end, we conduct experiments regarding brain tumor segmentation from multimodal slices extracted from MRI volumes, specifically focusing on whole-tumor segmentation, one of the tasks of the original challenge. We define the more appropriate UNet [58] in the hypercomplex domain, i.e. PHUNet, and set the parameter $n = 2$ considering the same modalities as for the OS prediction. The two models in the real and hypercomplex domain yield a very similar Dice score average of about 83% on BraTS19 [41], as reported in Tab. VII, proving the validity of the proposed approach also for finer-scaled tasks. Moreover, we believe these results can be further improved in future works that mainly focus on tasks such as detection and segmentation, employing more complex networks and extending to a 3D segmentation scenario.

VII. VISUALIZING MULTI-VIEW LEARNING

In this section, we provide a visualization of how the hypercomplex models are able to model information from different views, depicted in Fig. 7. Specifically, we employ our best-performing model PHYSEnet and compare it against its real-valued counterpart SEnet. We consider a patient from INbreast with a benign finding in the left breast and a malignant mass in the right breast. We show the activation maps at two different levels of the architecture, i.e., after the encoder and after the refiner blocks (classifier). We obtain the activation maps by computing the average of feature channels. Regarding the

left views, by observing the activation maps of PHYSEnet, especially at the encoder level, we can see how it has learned a more focused representation, as the regions corresponding to the benign calcification are highlighted. While in the maps of SEnet, all areas of the breast are accentuated. But most importantly, in the right views the multi-view learning ability of the hypercomplex model is more visible. In fact, from the activation maps of PHYSEnet, it is clear that the network is learning from both views, as two areas are highlighted, corresponding to the location of the mass in the CC view and the MLO view. On the other hand, in the activation maps of SEnet, only one highlighted area appears, corresponding to the CC view only. Thus, it seems that the real model, unlike the PH network, is relying on only one view, not truly leveraging both views, as it also appears from Fig. 1. Moreover, sometimes a mass is visible only in one of the two views [3], [6]. In these situations, if the network has predominantly learned to depend on information from just one view, e.g., the CC view, it might misclassify cases where the mass is exclusively visible in the other view, e.g., the MLO view. This challenge is commonly encountered in multi-view breast cancer analysis, as elaborated in Section II and documented in the existing literature [5], [19]. Precisely for this reason, we propose the use of hypercomplex algebra to address this issue and enable the network to effectively learn from both views without overfitting to one view type.

Finally, for the hypercomplex network, we additionally compute the saliency map in Fig. 7. Moreover, we provide saliency maps and visualizations obtained with Grad-CAM [59] for different patients in Fig. 8, comparing the real-valued SEnet against its hypercomplex respective PHYSEnet. Saliency maps are computed for each side separately, using gradients of the class-dependent output over the input [60] in order to visualize which area of the two-view input is most influential for the model decision. By looking at the last column of Fig. 7 we can see in the right side the highlighted pixels that indeed correspond to the malignant mass, while

TABLE VIII

MODELS USE CASES SUMMARY. THE TICKS ✓ MEAN THAT THE MODEL CAN BE ADOPTED IN THE SPECIFIC CASE IF OUR PRETRAINED WEIGHTS ARE EMPLOYED. THIS IS BECAUSE WITHOUT ROI ANNOTATIONS IT IS NOT POSSIBLE TO TRAIN A PATCH CLASSIFIER, THUS THE PRETRAINING STAGE CANNOT BE PERFORMED.

Use Cases	PHResNet18	PHResNet50	PHYBOnet	PHYSEnet
Single View	✓	✓	✗	✗
Two Views	✓	✓	✗	✗
Four Views	✗	✗	✓	✓
ROI available	✓	✓	✓	✓
ROI not available	✓	✓	✓	✓
Light memory	✓	✗	✓	✗
Small size dataset	✓	✓	✓	✓
Other problems	✓	✓	✓	✓

the left-side map is darker and no pixel region is particularly accentuated since there are no malignant findings in the left breast. Interestingly, the maps for the left side differ between activation maps and saliency maps. This point highlights how the learned representation, visualized as activation maps, leverages patient-level information, i.e. from both sides, while the classification decision visualized in the saliency map has no highlighted area as the left view is classified as benign. In conclusion, by considering two well-established explainable techniques in Fig. 8, we further validate the visualizations provided in Fig. 1 and Fig. 7. In fact, also from these maps, it is evident how the proposed approach has the ability to effectively model local relations between views. On the contrary, the real-valued network seems to overfit on the CC view, which is indeed a typical behavior and challenge encountered in the literature [19] that we specifically address in this paper through our hypercomplex architectures.

VIII. HOW DO I CHOOSE THE BEST MODEL FOR MY DATA?

In this section, we aim at answering the reader question *Which model do I employ on my data and for my problem?*

We consider multiple scenarios, including datasets with 1, 2, or 4 views, whether ROI annotations are available or not, the memory constraints, the size of the dataset, and whether the proposed models are easily exportable to other kinds of medical imaging problems. Table VIII reports the applicability of each network we propose in the above-mentioned scenarios. In detail, the main difference between PHYBOnet and PHYSEnet lies in their complexity and parameter count. PHYBOnet is designed as a lightweight model comprising only 7 million parameters. Despite its reduced complexity, PHYBOnet exhibits competitive performance, as demonstrated by the experimental results shown in Section VI-C2. In contrast, PHYSEnet is a more intricate model with 20 million parameters that stands out as the top-performing model among all the networks tested, as indicated in Section VI-C2. In summary, the main advantage of PHYBOnet is its lightweight nature, which allows it to be computationally efficient while still delivering competitive results thanks to the ability to exploit both global and local relations. While PHYSEnet, with its larger parameter count and the same ability, excels in terms of performance. Moreover, while we prove the crucial role of pretraining for breast cancer classification tasks, especially when only scarce data is available, this is only applicable in the

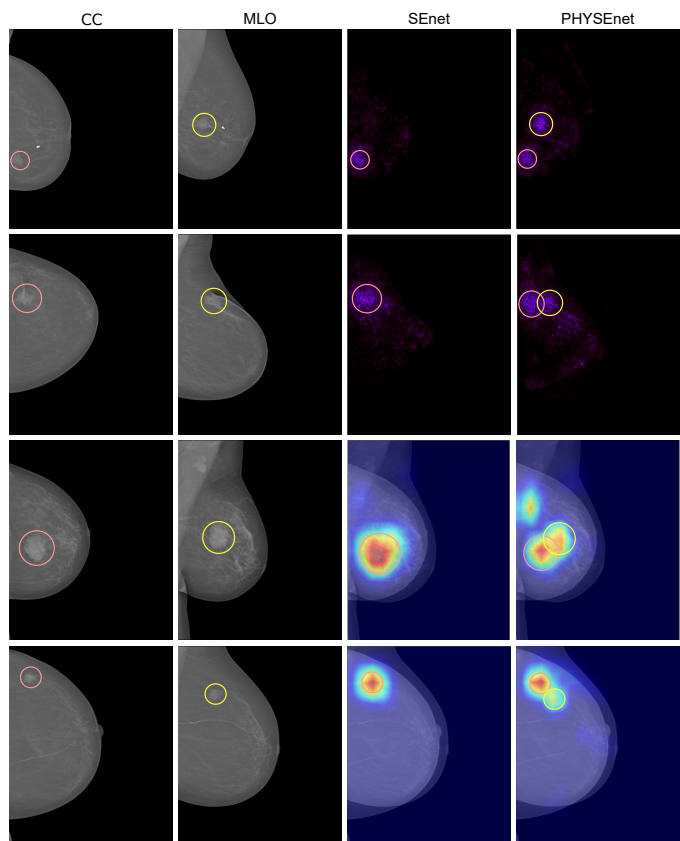


Fig. 8. Saliency and Grad-CAM maps of different patients. Circles indicate malignant masses, while red and yellow correspond to the CC and MLO view, respectively. We show the saliency maps and visualizations obtained with Grad-CAM of SEnet and PHYSEnet. By looking at the highlighted areas, it is visible from both explainability techniques that the hypercomplex network effectively models local relations, i.e. the complementary information contained in the two views, unlike its real-valued counterpart.

case of datasets with provided ROI annotations. Nevertheless, our methods can be applied even in datasets where ROI observations are missing, since we provide pretrained models and weights¹ to overcome this limitation. We believe that Table VIII may help the reader clarify which model better fits specific cases and may increase the usability of our approach in future research and in different medical fields.

¹Weights are freely available at <https://github.com/ispamm/PHBreast>

IX. CONCLUSIONS

In this paper, we have introduced an innovative approach for breast cancer classification that handles multi-view mammograms as radiologists do, thus leveraging information contained in ipsilateral views as well as bilateral. Thanks to hypercomplex algebra properties, neural models are endowed with the capability of capturing and truly exploiting correlations between views and thus outperforming state-of-the-art models. At the same time, we demonstrate how our approach generalizes considering different imaging exams as well as proving its efficacy on finer-scaled tasks, while also being flexible to be adopted in any existing neural network. For future work, it would be interesting to extend to an unsupervised learning scenario and expand the work done on finer-scaled tasks considering more recent models, such as transformer-based networks. We believe that our approach is a real breakthrough for this research field and that it may pave the way to novel methods capable of processing medical imaging exams with techniques closer to radiologists and to human understanding.

REFERENCES

- [1] R. L. Siegel, K. D. Miller, H. E. Fuchs, and A. Jemal, "Cancer statistics, 2022," *CA: A Cancer Journal for Clinicians*, vol. 72, no. 1, pp. 7–33, 2022.
- [2] I. C. Moreira, I. Amaral, I. Domingues, A. Cardoso, M. J. Cardoso, and J. S. Cardoso, "INbreast: Toward a full-field digital mammographic database," *Academic Radiology*, vol. 19, no. 2, pp. 236–248, 2012.
- [3] S. Misra, N. L. Solomon, F. L. Moffat, and L. G. Koniaris, "Screening criteria for breast cancer," *Adv. Surg.*, vol. 44, pp. 87–100, 2010.
- [4] D. Gur, G. S. Abrams, D. M. Chough, M. A. Ganott, C. M. Hakim, R. L. Perrin, G. Y. Rathfon, J. H. Sumkin, M. L. Zuley, and A. I. Bandos, "Digital breast tomosynthesis: Observer performance study," *American Journal of Roentgenology*, vol. 193, no. 2, pp. 586–591, 2009.
- [5] Y. Liu, F. Zhang, C. Chen, S. Wang, Y. Wang, and Y. Yu, "Act like a radiologist: Towards reliable multi-view correspondence reasoning for mammogram mass detection," *IEEE Trans. Pattern Anal. Mach. Intell.*, no. 01, pp. 1–1, 2021.
- [6] L. Shen, L. Margolies, J. Rothstein, E. Fluder, R. McBride, and W. Sieh, "Deep learning to improve breast cancer detection on screening mammography," *Sci. Rep.*, vol. 9, 2019.
- [7] N. Wu, Z. Huang, Y. Shen, J. Park, J. Phang, T. Makino, S. Kim, K. Cho, L. Heacock, L. Moy, and K. J. Geras, "Reducing false-positive biopsies using deep neural networks that utilize both local and global image context of screening mammograms," *Journal of Digital Imaging*, vol. 34, pp. 1414 – 1423, 2021.
- [8] G. Murtaza, L. Shuib, A. Wahid, G. Mujtaba, H. Nweke, M. Al-Garadi, F. Zulfiqar, G. Raza, and N. Azmi, "Deep learning-based breast cancer classification through medical imaging modalities: state of the art and research challenges," *Artificial Intelligence Review*, vol. 53, 03 2020.
- [9] D. Abdelhafiz, C. Yang, R. Ammar, and S. Nabavi, "Deep convolutional neural networks for mammography: advances, challenges and applications," *BMC Bioinformatics*, vol. 20, 2019.
- [10] S. S. Aboutalib, A. A. Mohamed, W. A. Berg, M. L. Zuley, J. H. Sumkin, and S. Wu, "Deep Learning to Distinguish Recalled but Benign Mammography Images in Breast Cancer Screening," *Clinical Cancer Research*, vol. 24, no. 23, pp. 5902–5909, 2018.
- [11] I. Sechopoulos and M. R. Mann, "Stand-alone artificial intelligence - the future of breast cancer screening?" *The Breast*, vol. 49, pp. 254–260, 2020.
- [12] M. A. Al-antari, M. A. Al-masni, and T.-S. Kim, "Deep learning computer-aided diagnosis for breast lesion in digital mammogram," *Adv. Exp. Med. Biol.*, vol. 1213, pp. 59–72, 2020.
- [13] R. Agarwal, O. Diaz, X. Lladó, M. H. Yap, and R. Martí, "Automatic mass detection in mammograms using deep convolutional neural networks," *Journal of Medical Imaging*, vol. 6, no. 3, pp. 1–9, 2019.
- [14] J. Niu, H. Li, C. Zhang, and D. Li, "Multi-scale attention-based convolutional neural network for classification of breast masses in mammograms," *Medical Physics*, vol. 48, no. 7, pp. 3878–3892, 2021.
- [15] G. Zhao, Q. Feng, C. Chen, Z. Zhou, and Y. Yu, "Diagnose like a radiologist: Hybrid neuro-probabilistic reasoning for attribute-based medical image diagnosis," *IEEE Trans. Pattern Anal. Mach. Intell.*, 2021.
- [16] H. Pinckaers, B. van Ginneken, and G. Litjens, "Streaming convolutional neural networks for end-to-end learning with multi-megapixel images," *IEEE Trans. Pattern Anal. Mach. Intell.*, vol. 44, no. 3, pp. 1581–1590, 2022.
- [17] C. Lian, M. Liu, J. Zhang, and D. Shen, "Hierarchical fully convolutional network for joint atrophy localization and alzheimer's disease diagnosis using structural MRI," *IEEE Trans. Pattern Anal. Mach. Intell.*, vol. 42, no. 4, pp. 880–893, 2020.
- [18] N. Wu, J. Phang, J. Park, Y. Shen, Z. Huang, M. Zorin, S. Jastrzebski, T. Fevry, J. Katsnelson, E. Kim, S. Wolfson, U. Parikh, S. Gaddam, L. Lin, K. Ho, J. Weinstein, B. Reig, Y. Gao, H. Toth, K. Pysarenko, A. Lewin, J. Lee, K. Airola, E. Mema, S. Chung, E. Hwang, N. Samreen, S. Kim, L. Heacock, L. Moy, K. Cho, and K. Geras, "Deep neural networks improve radiologists' performance in breast cancer screening," *IEEE Trans. Med. Imaging*, vol. 39(4), 2020.
- [19] N. Wu, S. Jastrzebski, J. Park, L. Moy, K. Cho, and K. Geras, "Improving the ability of deep neural networks to use information from multiple views in breast cancer screening," in *Proc. of the Third Conf. on Med. Imaging with Deep Learning*, vol. 121. PMLR, 2020, pp. 827–842.
- [20] C. Zhang, J. Zhao, J. Niu, and D. Li, "New convolutional neural network model for screening and diagnosis of mammograms," *PLoS ONE*, vol. 15(8), 2020.
- [21] T. Kyono, F. J. Gilbert, and M. van der Schaar, "MAMMO: A deep learning solution for facilitating radiologist-machine collaboration in breast cancer diagnosis," *arXiv preprint: arXiv:1811.02661*, 2018.
- [22] —, "Triage of 2D mammographic images using multi-view multi-task convolutional neural networks," *ACM Trans. Comput. Healthcare*, vol. 2, no. 3, 2021.
- [23] —, "Multi-view multi-task learning for improving autonomous mammogram diagnosis," in *Proceedings of the 4th Machine Learning for Healthcare Conference*, ser. Proceedings of Machine Learning Research, vol. 106. PMLR, 2019, pp. 571–591.
- [24] L. Sun, J. Wang, Z. Hu, Y. Xu, and Z. Cui, "Multi-view convolutional neural networks for mammographic image classification," *IEEE Access*, vol. 7, pp. 126 273–126 282, 2019.
- [25] J. Song, Y. Zheng, M. Z. Ullah, J. Wang, Y. Jiang, C. Xu, Z. Zou, and G. Ding, "Multiview multimodal network for breast cancer diagnosis in contrast-enhanced spectral mammography images," *International Journal of Computer Assisted Radiology and Surgery*, vol. 16, pp. 979 – 988, 2021.
- [26] G. Carneiro, J. C. Nascimento, and A. P. Bradley, "Unregistered multi-view mammogram analysis with pre-trained deep learning models," in *Int. Conf. on Medical Image Computing and Computer Assisted Intervention (MICCAI)*, 2015.
- [27] J. Ma, X. Li, H. L., Ruixuan, W. Ruixuan, B. Menze, and W. Zheng, "Cross-View relation networks for mammogram mass detection," in *2020 25th International Conference on Pattern Recognition (ICPR)*, 2021, pp. 8632–8638.
- [28] Z. Yang, Z. Cao, Y. Zhang, Y. Tang, X. Lin, R. Ouyang, M. Wu, M. Han, J. Xiao, L. Huang, S. Wu, P. Chang, and J. Ma, "MommiNet-v2: Mammographic multi-view mass identification networks," *Medical Image Analysis*, vol. 73, p. 102204, 2021.
- [29] T. Baltrušaitis, C. Ahuja, and L.-P. Morency, "Multimodal machine learning: A survey and taxonomy," *IEEE Trans. Pattern Anal. Mach. Intell.*, vol. 41, no. 2, pp. 423–443, 2019.
- [30] W. Wang, D. Tran, and M. Feiszli, "What makes training multi-modal classification networks hard?" in *2020 IEEE/CVF Conf. on Computer Vision and Pattern Recognition (CVPR)*, 2020, pp. 12 692–12 702.
- [31] C. Gaudet and A. Maida, "Deep quaternion networks," in *IEEE Int. Joint Conf. on Neural Netw. (IJCNN)*, Rio de Janeiro, Brazil, Jul. 2018.
- [32] T. Parcollet, M. Morchid, and G. Linarès, "A survey of quaternion neural networks," *Artif. Intell. Rev.*, Aug. 2019.
- [33] T. Parcollet, M. Ravanelli, M. Morchid, G. Linarès, C. Trabelsi, R. De Mori, and Y. Bengio, "Quaternion recurrent neural networks," in *Int. Conf. on Learning Representations (ICLR)*, New Orleans, LA, May 2019, pp. 1–19.
- [34] D. Comminiello, M. Lella, S. Scardapane, and A. Uncini, "Quaternion convolutional neural networks for detection and localization of 3D sound events," in *IEEE Int. Conf. on Acoust., Speech and Signal Process. (ICASSP)*, Brighton, UK, May 2019, pp. 8533–8537.
- [35] M. Ricciardi Celsi, S. Scardapane, and D. Comminiello, "Quaternion neural networks for 3D sound source localization in reverberant environments," in *IEEE Int. Workshop on Machine Learning for Signal Process. (MLSP)*, Espoo, Finland, Sep. 2020, pp. 1–6.

- [36] C. Brignone, G. Mancini, E. Grassucci, A. Uncini, and D. Comminiello, "Efficient sound event localization and detection in the quaternion domain," *IEEE Trans. on Circuits and Systems II: Express Brief*, vol. 69, no. 5, pp. 2453–2457, 2022.
- [37] A. Zhang, Y. Tay, S. Zhang, A. Chan, A. T. Luu, S. C. Hui, and J. Fu, "Beyond fully-connected layers with quaternions: Parameterization of hypercomplex multiplications with $1/n$ parameters," *Int. Conf. on Machine Learning (ICML)*, 2021.
- [38] E. Grassucci, A. Zhang, and D. Comminiello, "PHNNs: Lightweight neural networks via parameterized hypercomplex convolutions," *IEEE Trans. on Neural Netw. and Learning Systems*, pp. 1–13, dec 2022.
- [39] R. Lee, F. Gimenez, A. Hoogi, M. Kanae, M. Gorovoy, and D. Rubin, "A curated mammography data set for use in computer-aided detection and diagnosis research," *Sci. Data*, vol. 4, 2017.
- [40] J. Irvin et al., "CheXpert: A large chest radiograph dataset with uncertainty labels and expert comparison," in *Proceedings of the AAAI conference on artificial intelligence*, vol. 33, no. 01, 2019, pp. 590–597.
- [41] B. H. Menze et al., "The multimodal brain tumor image segmentation benchmark (BRATS)," *IEEE Trans. on Med. Imaging*, no. 10, pp. 1993–2024, 2015.
- [42] S. Bakas, H. Akbari, A. Sotiras, M. Bilello, M. Rozycki, J. S. Kirby, J. B. Freymann, K. Farahani, and C. Davatzikos, "Advancing the cancer genome atlas glioma MRI collections with expert segmentation labels and radiomic features," *Scientific data*, vol. 4, no. 1, pp. 1–13, 2017.
- [43] H. N. Khan, A. R. Shahid, B. Raza, A. H. Dar, and H. Alquhayz, "Multi-view feature fusion based four views model for mammogram classification using convolutional neural network," *IEEE Access*, vol. 7, pp. 165 724–165 733, 2019.
- [44] S. R. Stahlschmidt, B. Ulfenborg, and J. Synnergren, "Multimodal deep learning for biomedical data fusion: a review," *Briefings in Bioinformatics*, vol. 23, no. 2, p. bbab569, 2022.
- [45] D. Ramachandram and G. W. Taylor, "Deep multimodal learning: A survey on recent advances and trends," *IEEE signal processing magazine*, vol. 34, no. 6, pp. 96–108, 2017.
- [46] M. E. Valle and R. A. Lobo, "Hypercomplex-valued recurrent correlation neural networks," *Neurocomputing*, vol. 432, pp. 111–123, 2021.
- [47] E. Grassucci, E. Cicero, and D. Comminiello, "Quaternion generative adversarial networks," in *Generative Adversarial Learning: Architectures and Applications*, R. Razavi-Far, A. Ruiz-Garcia, V. Palade, and J. Schmidhuber, Eds. Cham: Springer International Publishing, 2022, pp. 57–86.
- [48] M. Raghu, C. Zhang, J. Kleinberg, and S. Bengio, "Transfusion: Understanding transfer learning for medical imaging," in *Proceedings of the 33rd International Conference on Neural Information Processing Systems (NIPS)*, 2019, p. 3347–3357.
- [49] K. Geras, S. Wolfson, S. Kim, L. Moy, and K. Cho, "High-resolution breast cancer screening with multi-view deep convolutional neural networks," *arXiv preprint: arXiv:1703.07047*, 2017.
- [50] S. Bakas et al., "Identifying the best machine learning algorithms for brain tumor segmentation, progression assessment, and overall survival prediction in the BRATS challenge," *arXiv preprint arXiv:1811.02629*, 2018.
- [51] R. Hermoza, G. Maicas, J. C. Nascimento, and G. Carneiro, "Post-hoc overall survival time prediction from brain MRI," in *IEEE 18th Int. Symp. on Biom. Imag. (ISBI)*, 2021, pp. 1476–1480.
- [52] D. P. Kingma and J. Ba, "Adam: A method for stochastic optimization," in *3rd International Conference on Learning Representations, ICLR 2015, San Diego, CA, USA, May 7-9, 2015, Conference Track Proceedings*, Y. Bengio and Y. LeCun, Eds., 2015. [Online]. Available: <http://arXiv.org/abs/1412.6980>
- [53] Y. S. Aurelio, G. M. De Almeida, C. L. de Castro, and A. P. Braga, "Learning from imbalanced data sets with weighted cross-entropy function," *Neural processing letters*, vol. 50, pp. 1937–1949, 2019.
- [54] J. M. Johnson and T. M. Khoshgoftaar, "Survey on deep learning with class imbalance," *Journal of Big Data*, vol. 6, no. 1, pp. 1–54, 2019.
- [55] K. He, X. Zhang, S. Ren, and J. Sun, "Deep residual learning for image recognition," in *IEEE/CVF Conf. on Computer Vision and Pattern Recognition (CVPR)*, 2016, pp. 770–778.
- [56] J. Rubin, D. Sanghavi, C. Zhao, K. Lee, A. Qadir, and M. Xu-Wilson, "Large scale automated reading of frontal and lateral chest X-rays using dual convolutional neural networks," *arXiv preprint: arXiv:1804.07839*, 2018.
- [57] Z. Yuan, Y. Yan, M. Sonka, and T. Yang, "Large-scale robust deep auc maximization: A new surrogate loss and empirical studies on medical image classification," in *IEEE Int. Conf. on Computer Vision (ICCV)*, 2021, pp. 3040–3049.
- [58] O. Ronneberger, P. Fischer, and T. Brox, "U-net: Convolutional networks for biomedical image segmentation," in *Medical Image Computing and Computer-Assisted Intervention (MICCAI)*. Springer International Publishing, 2015, pp. 234–241.
- [59] R. R. Selvaraju, M. Cogswell, A. Das, R. Vedantam, D. Parikh, and D. Batra, "Grad-CAM: Visual explanations from deep networks via gradient-based localization," in *IEEE Int. Conf. on Computer Vision (ICCV)*, 2017, pp. 618–626.
- [60] K. Simonyan, A. Vedaldi, and A. Zisserman, "Deep inside convolutional networks: Visualising image classification models and saliency maps," *arXiv preprint arXiv:1312.6034*, 2013.